Electrochimica Acta 535 (2025) 146706

Contents lists available at ScienceDirect

Electrochimica Acta

journal homepage: www.journals.elsevier.com/electrochimica-acta

Amorphous surface modification and scalability of WO_3 nanostructures for photoelectrocatalytic degradation of organic pollutants

M. Cifre-Herrando [a], G. Roselló-Márquez [a,b], J. García-Antón [a,*], L. Mais [c], M. Mascia [c]

[a] Ingeniería Electroquímica y Corrosión (IEC), Instituto Universitario de Seguridad Industrial, Radiofísica y Medioambiental (ISIRYM), Universitat Politècnica de València, C/ Camino de Vera s/n, 46022 Valencia, Spain
[b] Departamento de Ingeniería Química, Universitat de València, Av. de les Universitats, s/n, 46100 Burjassot, Spain
[c] Università degli studi di Cagliari, Dipartimento di Ingegneria Meccanica, Chimica e dei Materiali, via Marengo 2, 09123 Cagliari, Italy

ARTICLE INFO

Keywords:
WO_3 nanostructures
Photoelectrocatalysis
Scalability
Diethyl phthalate
Water treatment

ABSTRACT

This work explores the use of WO_3 nanostructures as an effective solution for the removal of emerging contaminants from water, specifically focusing on the degradation of diethyl phthalate (DEP), a widely recognized environmental pollutant. A key aspect of the study is the scaling of the electrochemically active area and surface modification of WO_3 nanostructures, progressing from 0.5 cm^2 to 2.5 cm^2, followed by a surface reduction treatment that induces amorphization and enhances their photoelectrocatalytic activity after applying a 5-minute reduction treatment. Scaling was further extended to 15 cm^2, with the 15 cm^2 nanostructures exhibiting the highest DEP degradation rate, achieving a degradation constant of 0.0988 h^{-1}. The study also investigates the effect of key operational parameters such as applied voltage (1 V and 1.5 V), contaminant concentration (10 ppm, 25 ppm and 100 ppm). Reusability was also tested, with optimal conditions identified as 10 ppm DEP, 1 V, and the ability to reuse the nanostructures up to three times. Finally, under these optimal conditions, the degradation of DEP was monitored, leading to the identification of ten intermediate products and the proposal of a degradation pathway, highlighting the potential of WO_3 for sustainable and efficient water treatment applications.

1. Introduction

The increasing prevalence of organic pollutants in water resources presents a critical environmental challenge, particularly due to the limited efficacy of conventional water treatment methods [1]. This issue has raised concerns about the long-term impact on both ecosystems and human health [2,3].

Among these contaminants, phthalates, widely used as plasticizers, have been identified as emerging pollutants due to their persistence and potential toxic effects [4]. Diethyl phthalate (DEP) was selected for this study due to its extensive use as a plasticizer and its classification as a high-priority pollutant. DEP is a short-chain phthalate commonly found in vinyl flooring, resins, lubricating oils, and a variety of personal care products, including cosmetics and fragrances [5]. This widespread application has led to DEP's persistent presence in aquatic environments, where it poses significant ecological and health risks [6]. Furthermore, DEP has been identified as an endocrine disruptor, capable of interfering with reproductive functions and inducing various health issues, such as developmental and hormonal imbalances in both human and wildlife populations [7–9]. Due to its endocrine-disrupting properties, DEP has been classified as a priority pollutant by the United States Environmental Protection Agency (USEPA) and is a listed as a substance under review by the European Chemicals Agency (ECHA) [8,10].

Given DEP's environmental persistence and resistance to conventional water treatment processes, advanced degradation methods such as advanced oxidation processes (AOPs) have been studied for its degradation [11]. Photoelectrocatalysis (PEC) has emerged as a promising AOP due to its potential for efficient degradation of organic pollutants [12,13]. It combines electrolytic and photocatalytic processes in which there is a control of the system potential which allows enhance the efficiency of the process. Several studies have reported that the combination of photocatalysis and electrocatalysis in photoelectrocatalytic systems results in a synergistic effect that enhances degradation efficiency beyond the sum of the individual processes [14,15]. This synergy becomes particularly relevant for large-scale applications, where process efficiency and stability are critical.

* Corresponding author.
E-mail address: jgarciaa@iqn.upv.es (J. García-Antón).

https://doi.org/10.1016/j.electacta.2025.146706
Received 24 February 2025; Received in revised form 2 June 2025; Accepted 11 June 2025
Available online 14 June 2025

In the photoelectrocatalytic (PEC) process, electron-hole pairs are generated when the semiconductor is irradiated with light energy greater than its band gap. The application of an external bias potential facilitates the separation of these charge carriers, with electrons moving toward the cathode. At the semiconductor surface, the holes (h^+) oxidize water or hydroxide ions (OH^-) to produce hydroxyl radicals (·OH). These highly reactive radicals serve as powerful oxidizing agents, breaking down organic pollutants in the solution.

Tungsten oxide (WO_3) has shown excellent properties to use as a photoanode owing to its stability, narrow bandgap, and visible light absorption capabilities [16]. Previous research has demonstrated the effectiveness of WO_3 nanostructures for degrading various organic pollutants highlighting its potential for advanced water treatment applications [17–19]. In this study, the tungsten trioxide (WO_3) nanostructures have undergone significant modifications to enhance their photoelectrocatalytic performance.

To address the challenge of applying photoelectrocatalysis at an industrial scale the electrode area was scaled up from 0.5 cm^2 to 15 cm^2 [20]. This scale-up is a critical step for bridging the gap between laboratory-scale experiments and industrial applications, aiming to maintain or enhance the photoelectrocatalytic efficiency of WO_3 for larger-scale water treatment processes. In addition to scaling up the electrode area, the surface of the WO_3 nanostructures was modified in order to enhance their photoelectrocatalytic properties. Previous studies have demonstrated that the material's crystal structure significantly affects its electrochemical properties, particularly the interplay between amorphous and crystalline phases [21–23]. Consequently, the effect of the crystallinity of the nanostructure is studied, and the nanostructures are optimized by introducing an amorphous phase on the crystalline surface of WO_3 through a reduction treatment. This surface modification introduces a disordered, amorphous layer, which enhances the photoelectrocatalytic performance by increasing the density of oxygen vacancies and surface defects. These defects serve as active sites, promoting charge separation and improving the adsorption of reactant molecules, thereby reducing the recombination rate of photogenerated electron-hole pairs. Therefore, the amorphous-crystalline WO_3 nanostructure combines a crystalline phase that promotes charge separation with an amorphous WO_3 disordered structure that increase the surface defects, thereby increasing the number of active sites for (·OH) [21–25]. This novel approach aims to boost the efficiency of WO_3-based photoanodes, making them more effective for the degradation of persistent organic pollutants in water treatment applications [26,27].

The effectiveness of the modified WO_3 electrodes was evaluated in the degradation of DEP as a model pollutant. Additionally, the influence of initial DEP concentration and applied voltage during the degradation process was systematically investigated. The degradation intermediates were identified using high-performance liquid chromatography coupled with mass spectrometry (HPLC-MS), providing insight into the degradation pathways.

In this framework, this study presents a novel approach for the degradation of DEP through photoelectrocatalytically modified WO_3 nanostructures. Our work not only demonstrates the feasibility of scaling up the WO_3 photoelectrocatalytic electrodes but also highlights the improved performance achieved through surface modification. This dual optimization represents a significant advancement in adapting WO_3-based photoelectrocatalysis for industrial-scale water treatment applications. Additionally, the study systematically evaluates key degradation parameters, such as initial DEP concentration and applied voltage, providing a comprehensive insight into DEP degradation pathways and contributing to the development of more effective and sustainable water remediation technologies.

2. Experimental section

2.1. Synthesis of WO_3 nanostructures

The synthesis of WO_3 nanostructures was performed via electrochemical anodization under hydrodynamic conditions. This method allows the production of nanostructures with high surface area, significantly enhancing their properties for photoelectrocatalytic applications [28]. First, the tungsten surface was conditioned by polishing and cleaning with ethanol. After that, the anodization was conducted in a two-electrode cell using a platinum wire as counter electrode. The electrolyte consisted of 1.5 M methanesulfonic acid and 0.1 M citric acid maintained at 50 °C. A constant voltage of 20 V was applied for 4 h while maintaining electrode rotation at 375 rpm to ensure uniform growth of the nanostructures. Finally, the samples underwent thermal treatment at 600 °C for 4 h in an oxidizing atmosphere to convert the amorphous structures into a crystalline phase. All the chemicals employed possessed an analytical grade and were acquired from Panreac and ultrapure water of 18.2 MΩ·cm resistivity was used to prepare all the experiments.

2.2. Scaling of WO_3 nanostructures

The scalability of WO_3 nanostructures was evaluated by increasing their anodization area from 0.5 cm^2 to 15 cm^2. Initial nanostructures synthesized on tungsten rods (99.5 % purity, 10 cm in length, and 8 mm in diameter) with a 0.5 cm^2 active area were scaled up to 2.5 cm^2 using tungsten foil as the substrate (>99.9 % purity, thickness 0.25 mm). After confirming that the properties were maintained at 2.5 cm^2, the electrode area was further scaled up to 15 cm^2, also using tungsten foil. To achieve the specific area, a mold was used to electrochemically anodize only the desired area.

2.3. Surface modification

To enhance the photoelectrocatalytic performance of the WO_3 nanostructures, a surface modification was performed by applying a reduction potential of −0.16 V (vs. Ag/AgCl) to the synthesized WO_3 nanostructures. The potential of −0.16 V (vs. Ag/AgCl) was selected to induce surface reduction, creating oxygen vacancies and electronic defects that enhance charge carrier dynamics and reactivity. This value ensures controlled amorphization without compromising the structural integrity of the WO_3 nanostructures [24]. The process was initially conducted on the 2.5 cm^2 nanostructures, with reduction times of 2, 5, and 15 min to identify the optimal conditions for defect generation. Given the promising results obtained at 5 min of reduction, the same treatment was applied to the scaled-up 15 cm^2 nanostructures, ensuring the preservation of enhanced activity at larger scales. This two-step scaling and optimization approach demonstrates the potential of WO_3 nanostructures for practical, large-scale environmental applications.

2.4. Characterization

The crystalline WO_3 nanostructures synthesized on 0.5 cm^2 tungsten rods have been extensively characterized in previous studies [17]. Instead, this study focuses on evaluating the impact of the surface modifications applied to the scaled-up nanostructures. To this end, field emission scanning electron microscopy (FE-SEM) was employed to analyze the surface morphology induced by the reduction treatment. The equipment used was a Zeiss Ultra 55 Scanning Electron Miscroscope at an acceleration potential of 3 kV. Additionally, X-ray diffraction (XRD) was used to assess the crystalline properties of the nanostructures after the surface modification. The equipment used was a Bruker D8AVANCE (Bruker, Billerica, MA, USA) diffractometer with a Cu radiation operating at 40 kV from 5 °C to 80 °C.

To determine the optimal reduction time, linear sweep voltammetry measurements were performed using an Autolab PGSTAT302N

potentiostat (Metrohm, Herisau, Switzerland) and a solar simulator (AM 1.5 conditions at 100 mW cm^2). A three-electrode cell setup was used, using an Ag/AgCl (3 M KCl) as a reference electrode, a platinum wire as a counter electrode, and the WO_3 nanostructures as a working electrode. The electrolyte used was 0.1 M H_2SO_4, to ensure the photostability of the electrode [29]. The potential was scanned from 0.2 V (vs. Ag/AgCl) to 1.5 V (vs. Ag/AgCl) at a scan rate of 2 mVs^{-1} under pulsed light conditions (60 s light off, 20 s light on). Additionally, stability tests were performed at 1.5 V (vs. Ag/AgCl) for 1 h to evaluate the long-term electrochemical performance of each nanostructure. This approach allowed for the identification of the optimal reduction time by determining which nanostructure exhibited the most pronounced photoresponse. Photoelectrochemical impedance spectroscopy (PEIS) measurements were carried out applying 1 VAg/AgCl in the frequency range varied from 100 kHz to 10 mHz with a 10 mV of amplitude.

2.5. Photoelectrochemical degradation

Photoelectrochemical (PEC) degradation tests were performed in a photoelectrochemical quartz reactor, maintaining a constant ratio of nanostructure area to reactor volume (0.004 $m^2 \cdot L^{-1}$) as the area of the nanostructures was scaled up.

The electrochemical cell configuration includes the WO_3 nanostructures as an anode (with an exposed area of 0.5 cm^2, 2.5 cm^2 and 15 cm^2. Different potentials (1 V and 1.5 V vs Ag/AgCl) were applied and A 1000 W Xenon lamp provided light at an intensity of 100 mW/cm^2, positioned 30 cm from the photoanode.

The degradation experiments were conducted using Diethyl phthalate (DEP) as the target contaminant at initial concentrations of 10 ppm, 25 ppm, and 100 ppm in 0.1 M H_2SO_4 to ensure acidic conditions and stability of the nanostructures. The degradation process was carried out at room temperature with magnetic stirring, and samples were taken hourly for 24 h.

To further evaluate the durability and reusability of the WO_3 nanostructures, their reuse was also assessed. After each degradation cycle, the nanostructures were thoroughly rinsed with deionized water, dried, and subjected to a subsequent degradation experiment under identical conditions.

Degradation was monitored using an Agilent 1290 Infinity Ultra-High-Performance Liquid Chromatography coupled with Time-of-Flight Mass Spectrometry (UHPLC-MS-Q-TOF). The UHPLC system used a C-18 column (50 mm × 2.1 mm, 1.8 μm particle size) in positive ionization mode (ESI+). The separation was achieved using solvent A (water with 0.01 % acetic acid) and solvent B (methanol) at a flow rate of 0.8 mL/min. The gradient was as follows: from 0 to 25 min, the composition was gradually changed from 80 % A to 10 % A; at 25–26 min, the composition was maintained at 10 % A; from 26 to 26.50 min, the conditions were returned to the initial state; and from 26.50 to 28 min, the system was equilibrated.

The total run time was under 30 min, with a column temperature of 30 °C and a sample volume of 2 μL. The mass spectrometer analyzed spectra within the *m/z* range of 50–1700, with optimized parameters: capillary voltage 4000 V, nebulizer pressure 45 psi, drying gas flow rate 11 L/min, and gas temperature 350 °C. Data analysis was performed using Agilent MassHunter Qualitative Analysis software.

3. Results and discussion

3.1. Scaling of WO_3 nanostructures and surface modification

To evaluate the scalability and efficiency of WO_3 nanostructures for degradation of contaminants, an initial scale-up was conducted, increasing the surface area of nanostructures from 0.5 cm^2 to 2.5 cm^2. As the WO_3 nanostructures initially synthesized on a tungsten bar with 0.5 cm^2 surface area were effective for contaminant degradation in previous studies [17], the scaling of these nanostructures was pursued to explore their viability for larger-scale applications. The objective of scaling is to confirm that the performance observed at smaller scales can be maintained or improved when applied to larger surface areas, which is essential for practical environmental applications such as wastewater treatment.

Consequently, nanostructures of 2.5 cm^2 surface area were synthesized and the photoelectrocatalytic degradation using these nanostructures was carried out for the degradation of the contaminant diethyl phthalate (DEP) under an applied voltage of 1 V and an initial contaminant concentration of 10 ppm.

The results of the degradation are shown in Table S1 and Fig. 1. The final degradation percentages achieved for both nanostructures, 0.5 cm^2 and 2.5 cm^2, are very similar (70 % with 0.5 cm^2 and 67 % with 2.5 cm^2) This result indicates that the larger 2.5 cm^2 surface area successfully retains a comparable degradation capacity, confirming that the scaling process did not adversely affect the catalytic efficiency of the nanostructures.

Fig. 1 shows the kinetic analysis of the degradation reaction for each nanostructure size, where the pseudo-first-order rate constants are derived from the linear fit of ln (C/Co) over time. The rate constants are $k = 0.0988\ h^{-1}$ for the 0.5 cm^2 nanostructure and $k = 0.062\ h^{-1}$ for the 2.5 cm^2 nanostructure. While the kinetic rate constant is slightly lower for the larger surface area, the comparable final degradation percentages demonstrate that the scaled-up nanostructure remains highly effective, as the constant area-to-volume ratio (4 m^{-1}) ensures that differences arise from intrinsic properties of the material rather than A/V variations.

The successful replication of degradation performance at a larger scale confirms the feasibility of scaling up WO_3 nanostructures for potential pilot-scale applications. This effective scaling is a promising step towards using these nanostructures in practical environmental applications, where larger surface areas are required to treat substantial volumes of contaminated water.

After increasing the surface area of the electrode, an optimization process was conducted to enhance their photoelectrocatalytic performance. This optimization involved studying the effect of crystallinity on the catalytic properties of the nanostructures by introducing an amorphous layer over the crystalline WO_3 surface through a reduction treatment. This involved applying a reduction potential of −0.16 V vs. Ag/AgCl (3 M KCl) to induce surface defects on the crystalline WO_3 structure [24]. This amorphization introduces a higher density of oxygen vacancies and electronic defects, which act as active sites and

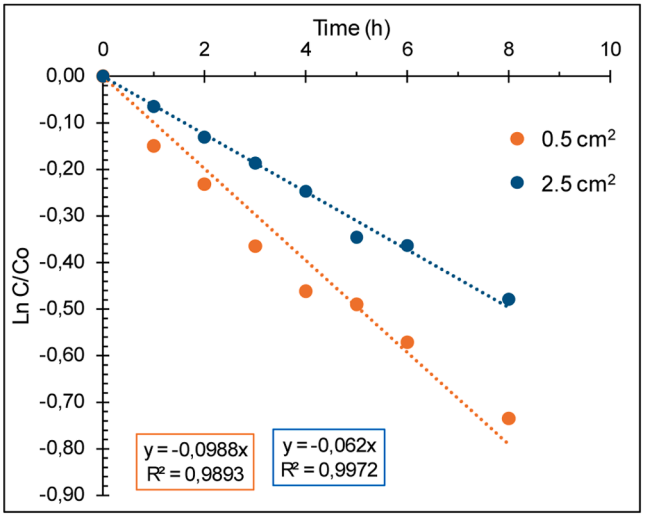

Fig. 1. Comparison of the photoelectrocatalytic degradation kinetics of DEP with nanostructures with 0.5 cm^2 surface are and 2.5 cm^2 applying 1 V and using 10 ppm as initial concentration.

improve charge carrier dynamics in the material. Oxygen vacancies are particularly beneficial because they can enhance the adsorption and activation of oxygen-containing species, thereby facilitating the degradation of contaminants like diethyl phthalate (DEP) [21,25–27].

The effect of the reduction treatment was studied at varying application times (2, 5, and 15 min) to determine the optimal conditions for defect generation. Fig. 2 presents the linear sweep voltammetry (LSV) curves of each nanostructure before and after applying a reduction potential of −0.16 V for different durations (2, 5, and 15 min), while Table 1 summarizes the current density differences, and percentage increase in current density for each nanostructure after the treatment [24]. The potential value of 1 V was chosen because this voltage corresponds to the saturation region for the photoanode in terms of photocurrent, as observed in the LSV curves shown in Fig. 2. This ensures that the measurements are representative of the material's maximum photocatalytic activity under the given conditions.

In the initial, untreated state, the photocurrent density reaches 0.200 mA/cm^2. After a 2-minute reduction treatment, the current increases to 0.283 mA/cm^2, achieving an improvement of 41.57 %, suggesting that the introduction of surface defects—along with potential changes in specific surface area—enhances photoelectrocatalytic activity. The best response is obtained with a 5-minute reduction treatment, where the current reaches 0.349 mA/cm^2, representing a 74.59 % improvement compared to the untreated sample. This suggests that a moderate defect formation optimally enhances charge separation and increases the number of active sites on the WO_3 surface, thereby boosting its photoelectrochemical performance. However, extending the reduction to 15 min results in a decrease in performance, with a photocurrent density of 0.146 mA/cm^2, a 26.96 % reduction compared to the initial state. This decline could be attributed to excessive defect formation, which may hinder charge transfer efficiency by introducing an unfavorable defect density or may deteriorate the surface of the nanostructure [30].

Additionally, stability tests over 1 h (Figure S1) show that the 5-minute reduction treatment not only provides the highest photocurrent but also maintains stable performance throughout the duration of the test. In contrast, the 15-minute treatment results in a decrease in photocurrent, confirming the optimal stability and electrochemical response for the 5-minute treatment.

In summary, a 5-minute reduction treatment at −0.16 V optimally enhances the photoelectrochemical response of WO_3 nanostructures, striking a balance between defect formation and structural integrity. This optimized treatment significantly improves the material's suitability for photoelectrocatalytic applications, such as organic contaminant degradation, by maximizing charge carrier efficiency and catalytic activity.

Table 1
Maximum photocurrent achieved (applying 1 V) for each nanostructure and improvement (%) of the photocurrent density with respect to the initial sample.

Sample	Photoelectrocatalytic Current (mA/cm^2)	Current density improvement (%)
No reduction	0.200	00.00
2	0.283	41.57
5	0.349	74.59
15	0.146	−26.96

To further analyze the effect of the reduction treatment over the surface of the nanostructures, the morphology of the WO_3 nanostructures was analyzed using Field Emission Scanning Electron Microscopy (FE-SEM), as shown in Fig. 3. The surface structure was examined in its initial state (without reduction) and after applying a reduction potential for different durations (2, 5, and 15 min).

The as-synthesized WO_3 nanostructures present a homogeneous layer of well-defined nanorods uniformly distributed across the surface. This initial morphology, with closely packed nanorods, reflects the crystalline structure typical of WO_3 before any reduction treatment [17]. After applying a reduction potential for 2 min, the morphology of the nanostructures begins to change. The nanorods appear to start aggregating, resulting in a slightly less uniform distribution. This initial modification indicates a trend towards a more porous morphology, which could potentially enhance the surface area. At 5 min of reduction, the WO_3 nanostructures undergo a significant morphological transformation. The surface becomes visibly more porous, with interconnected nanorods creating a rougher and more open network. This enhanced porosity, in conjunction with the partial disruption of the crystalline structure, is likely to improve the photocatalytic and electrochemical activity by increasing the active surface area and facilitating greater interaction with the diethyl phthalate (DEP) molecules. Finally, extending the reduction time to 15 min leads to visible degradation of the surface structure. The nanostructures lose much of their porosity, and the morphology appears deteriorated, with less defined features and fewer interconnected nanorods. This deterioration suggests a collapse or excessive reduction of the nanostructures, resulting in a decrease in the active surface area.

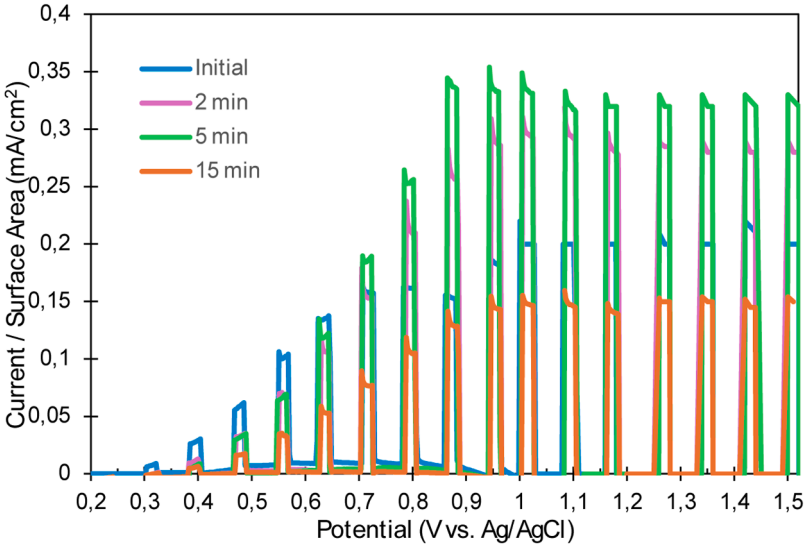

Fig. 2. LSV curves with light and dark pulses of each nanostructure (initial nanostructure and after the reduction treatment applied for 2 min, 5 min and 15 min) obtained with a surface area of 2.5 cm^2.

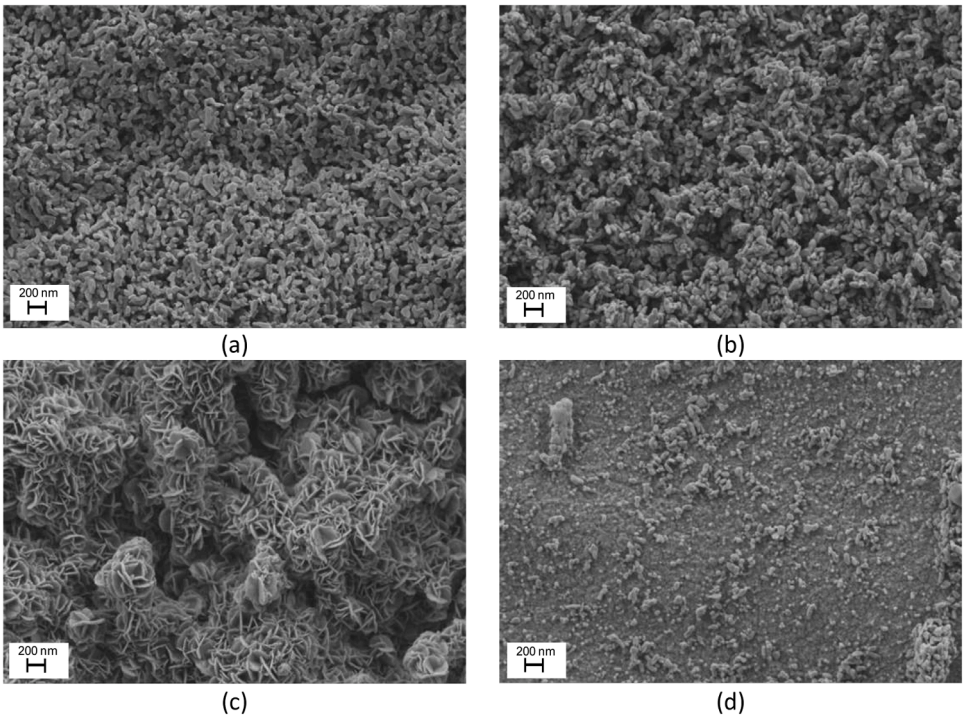

Fig. 3. FE-SEM images of the WO_3 nanostructures obtained with an area of 2.5cm^2 (a) crystalline structure – original and after the reduction treatment for (b) 2 min, (c) 5 min and (d) 15 min.

Additionally, FE-SEM analysis of electrodes with different geometric areas (0.5 cm^2 and 15 cm^2), shown in Figure S2, confirmed that the nanostructure morphology remains consistent across scales when synthesized and treated under the same conditions, supporting the reproducibility and scalability of the process.

These observations are consistent with the results of the LSV, indicating that a reduction time of 5 min is optimal for enhancing the surface morphology of WO_3 nanostructures for photoelectrocatalytic degradation applications. At this duration, the nanostructures achieve a morphology with an ideal balance of porosity and surface area, maximizing their catalytic efficiency. Therefore, from the results obtained so far, the nanostructure with 5 min of reduction treatment (amorphous nanostructure) will be further studied and compared with the initial nanostructure without reduction treatment (crystalline nanostructure). For clarity throughout the manuscript, we will refer to the initial nanostructure as the crystalline nanostructure, and to the electrochemically reduced one as the amorphous nanostructure

X-ray diffraction (XRD) has been carried out to identify the crystallinity of the samples. XRD patterns of the crystalline and the amorphous (after 5 min of reduction) nanostructure are presented in Fig. 4.

The original WO_3 sample exhibits a mixed-phase structure characteristic of monoclinic WO_3. This is evidenced by prominent diffraction peaks at approximately 23.1°, 23.52° and 48.10° in the original sample, corresponding to the (002), (020) and (220) planes, respectively [31–33]. Upon reduction (amorphous nanostructure), the XRD pattern of the sample reveals significant structural changes, the peaks corresponding to the monoclinic WO_3 still appear but, only the (020) and (220) at 23.2°and 47.7°, with a shift in the primary diffraction peaks, consistent with the transformation to a hydrogenated tungsten oxide phase [24]. The reduced sample displays diffraction peaks that are

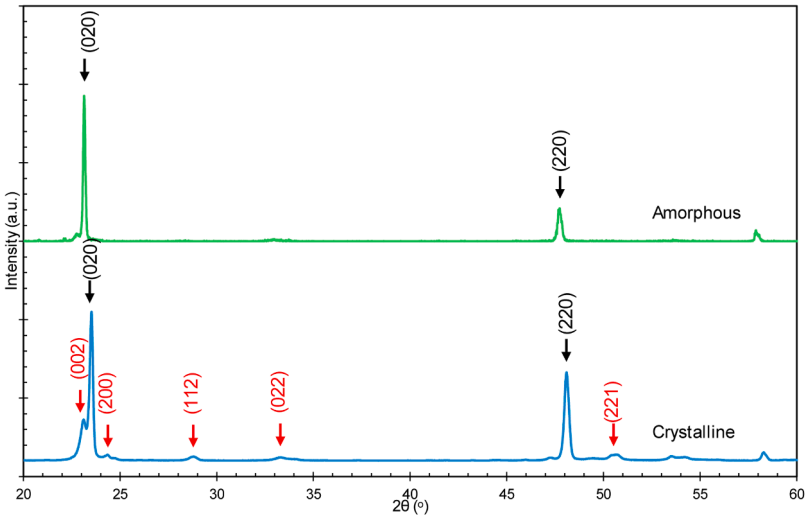

Fig. 4. XRD patterns of the original sample (crystalline) and the reduced WO_3 sample for 5 min (amorphous).

characteristic of the tetragonal $H_{0.23}WO_3$ phase, particularly evidenced by the shift of the main peak to align with the (020) plane [34]. This shift is attributed to the electrochemical insertion of H^+ ions into the WO_3 lattice, a process which fills the oxygen vacancy sites and further increases the charge carrier concentration within the material [24]. Furthermore, the comparison of relative peak intensities between the original and reduced samples further supports the transformation from the crystalline to the amorphous phase. Notably, several characteristic peaks of monoclinic WO_3 present in the original (crystalline) sample—highlighted in red—corresponding to the (002), (200), (112), (022), and (221) planes, disappear in the reduced sample. This loss of distinctive monoclinic WO_3 peaks confirms the transition to an amorphous structure upon reduction, reflecting significant structural reorganization. This structural modification is essential for optimizing the material's photoelectrocatalytic performance, as hydrogenation of WO_3 has been shown to significantly increase both surface reactivity and photoelectrochemical response due to the introduction of additional charge carriers [34,35].

The XRD results confirm that the reduction process induces a transition from a well-ordered monoclinic crystalline structure to a partially amorphous hydrogenated phase, introducing significant structural reorganization. This transition is closely linked to the observed morphological changes, where the formation of a more porous structure (as seen in FE-SEM images, Fig. 3) corresponds to a progressive loss of long-range crystallinity. The increased porosity and the loss of distinct monoclinic peaks suggest the generation of a higher density of surface defects, which can enhance the specific surface area. These defects, particularly oxygen vacancies, act as active sites for charge transfer and catalytic reactions, improving the material's overall photoelectrocatalytic (PEC) efficiency.

In addition, photoelectrochemical impedance spectroscopy (PEIS) measurements were performed to further investigate the charge transfer characteristics of the different WO_3 structures. The results, shown in Figure S3 and discussed in the Supplementary Material, reveal a noticeable decrease in charge transfer resistance for the amorphous WO_3, consistent with the presence of more active sites and improved interfacial kinetics.

To validate these hypotheses, the optimized WO_3 nanostructures were tested as photoanodes for the photoelectrocatalytic degradation of DEP under an applied potential of 1 V and an initial contaminant concentration of 10 ppm. Fig. 5 compares the degradation performance of the crystalline and amorphous WO_3 nanostructures, providing direct evidence of the beneficial impact of increased defect density and specific surface area on photocatalytic activity.

The degradation results reveal a clear difference between the crystalline (without reduction treatment) and amorphous (after 5 min of reduction) WO_3 nanostructures. The amorphous nanostructure demonstrates a significantly higher initial degradation rate, achieving nearly 90 % degradation after 24 h. This suggests that the amorphous structure, enriched with surface defects and oxygen vacancies due to the reduction process, provides more active sites, facilitating faster degradation reactions. In contrast, the crystalline structure shows a slower degradation rate, reaching around 70 % degradation after 24 h. Fig. 5 shows the kinetic analysis adjusted to a pseudo-first order kinetic. The amorphous structure has a steeper slope, with a rate constant of $-0.124\ h^{-1}$, compared to $-0.062\ h^{-1}$ for the crystalline one. This further confirms the superior efficiency of the amorphous nanostructure in the photocatalytic degradation process, likely due to enhanced charge separation and increased catalytic activity from the defect-rich surface.

Following the scaling process of the nanostructures, the area has been increased from 2.5 cm^2 to 15 cm^2. Consequently, nanostructures of WO_3 with an active area of 15 cm^2 have been synthesized and the process included the application of a reduction treatment for 5 min at a potential of −0.16 V, in order to induce defects in the WO_3 structure. These WO_3 nanostructures were used as photoanodes in the DEP degradation process.

Fig. 6 presents the comparative graphs of DEP degradation employing amorphous WO_3 nanostructures of 2.5 cm^2 and the scaled-up area of 15 cm^2, showing the degradation percentage and kinetic behavior as a function of reaction time. For the 2.5 cm^2 amorphous nanostructure, it was observed that DEP degradation reached 85.44 % after 24 h of reaction, with a rate constant (k) of 0.0988 h^{-1}, while for the degradation with 15 cm^2, DEP degradation reached 97.18 % after 24 h, with a rate constant (k) of 0.0995 h^{-1}. These results indicate that, as the area of the photoanode increased, with the A/V ratio kept constant, the efficiency of the degradation process was maintained and even slightly improved, which is evidence that the scaling of the nanostructure does not compromise the effectiveness of the treatment.

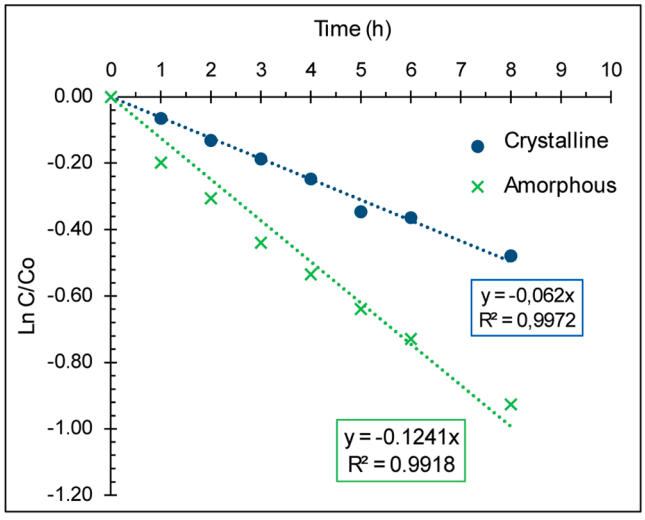

Fig. 5. Photoelectrocatalyc degradation kinetics with the 2.5 cm^2 nanostructure and comparison of the initial nanostructure without reduction treatment (crystalline) and the nanostructure after 5 min reduction treatment (amorphous) under an applied potential of 1 V and an initial concentration of 10 ppm.

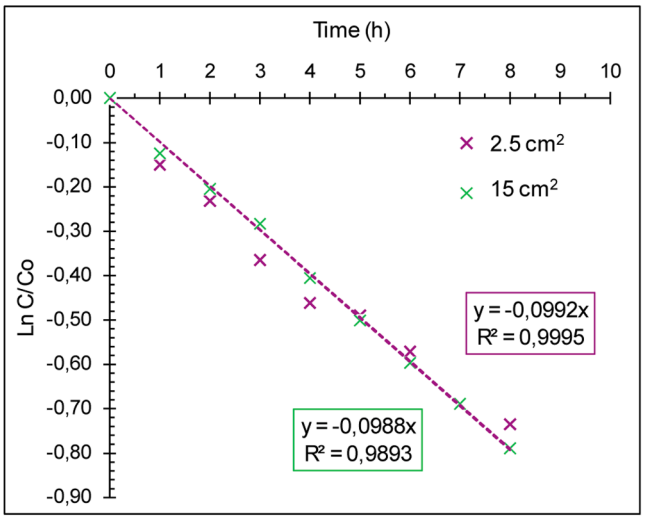

Fig. 6. Photoelectrocatalyc degradation kinetics of DEP with an initial concentration of 10 ppm applying 1 V with the amorphous nanostructure synthesized at different areas: 2.5 cm^2 and 15 cm^2.

3.2. Photoelectrochemical degradation of DEP varying different parameters

After achieving the successful scaling of WO_3 nanostructures to 15 cm^2 and the modification of the surface, we proceeded to investigate the degradation efficiency of diethyl phthalate (DEP) varying different parameters to evaluate their influence on the degradation percentage after 24 h and the reaction rate constant. We choose as our study parameters the initial contaminant concentrations (10 ppm, 25 ppm and 100 ppm) and the applied voltage during degradation (1 V and 1.5 V).

Different degradations were carried out varying these parameters. Fig. 7 presents the degradation results for three initial concentrations of DEP (10, 25, and 100 ppm) with varying voltage (1 V and 1.5 V). Table S2 summarizes the kinetic coefficients obtained under each condition.

Comparing the effect of applied voltage and initial DEP concentration, we observe distinct trends. At lower concentrations (10 and 25 ppm), increasing the voltage from 1.0 to 1.5 V slightly reduces the reaction rate constant: for 10 ppm, k decreases from 0.1301 h^{-1} to 0.0992 h^{-1}, and for 25 ppm, from 0.1274 h^{-1} to 0.0969 h^{-1}. This suggests that 1.0 V is optimal, as a higher voltage does not enhance degradation efficiency and may introduce overpotential effects that lower performance.

As reported in the literature for similar systems, the mass transfer coefficient (akm) value can be assumed to be 0.072 h^{-1}, confirming that for diluted solutions, akm is always lower than the kinetic constant [36]. At these low concentrations, the system operates under mass transfer control, meaning that the process is limited by the availability of reactive species rather than by the applied voltage. While increasing the voltage raises the current density, it does not significantly impact the degradation rate because the system is already constrained by mass transfer limitations. In diluted solutions, the concentration of oxidizing agents on the anode surface is much higher than the amount of DEP reaching it. Additionally, the short lifetime of hydroxyl radicals promotes the formation of hydrogen peroxide or the oxygen evolution reaction, leading to a subsequent reduction in current efficiency. This behavior is consistent with previous studies, which have shown that in electrochemical systems with low pollutant concentrations, the removal process is mainly limited by the availability of reactive species (ROS) rather than operational parameters [37,38].

On the other hand, in concentrated solutions (100 ppm), the process is kinetically controlled: the degradation rate constant is significantly lower than at lower concentrations, but it improves when the voltage increases from 1.0 to 1.5 V (from 0.0409 h^{-1} to 0.0708 h^{-1}). This suggests that at high pollutant loads, the system may experience a saturation effect due to limited ROS availability, and applying a higher voltage helps partially overcome this limitation. Therefore, while 1 V is optimal for moderate DEP concentrations, 1.5 V enhances degradation efficiency in highly contaminated scenarios.

This phenomenon aligns with previous findings on phenol degradation, which indicate that at higher contaminant concentrations, the cell's electrical resistance increases due to the saturation of active oxidation sites [37]. The saturation effect occurs because the contaminant occupies the active sites on the electrode, reducing the efficiency of the oxidation process. Increasing the voltage boosts the current density, which partially compensates for the ROS depletion, improving contaminant degradation. Similarly, in the present study, increasing the voltage from 1 V to 1.5 V at an initial concentration of 100 ppm helps to enhance ROS availability, improving degradation efficiency despite the high pollutant load.

Overall, while DEP degradation at 10–25 ppm follows pseudo-first-order kinetics with minimal influence from initial concentration, at 100 ppm, ROS depletion becomes a critical factor. In this photoelectrochemical system, the balance between pollutant load and ROS availability dictates the optimal operational conditions: 1.0 V is sufficient for lower concentrations, whereas 1.5 V enhances degradation at high pollutant loads.

Furthermore, to clarify the role of light and applied potential, additional control experiments were performed under dark conditions (electrocatalysis) using an initial concentration of 100 ppm of diethyl phthalate, at both applied potentials 1.0 V and 1.5 V vs. Ag/AgCl. The results are included in the Supplementary Material as Figure S4. The results confirmed that photoelectrocatalysis leads to significantly higher degradation efficiency than either process alone, demonstrating a synergistic effect between light and potential [14,15].

3.3. Reusability tests

To further evaluate the stability and reusability of the synthesized WO_3 nanostructures, a reusability test was conducted by repeating the DEP degradation process three times with the same nanostructure and measuring the degradation percentage and kinetic constant after each cycle. The test was performed using the optimized WO_3 nanostructures, those with a 5-minute reduction treatment and a surface area of 15 cm^2, which provided the ideal properties for the degradation process. The degradation was carried out using the optimum conditions: 10 ppm as initial concentration of DEP and applying 1 V (Fig. 8).

The reuse study of the WO_3 nanostructured anodes demonstrates promising stability and reusability in the photoelectrochemical degradation of DEP. Analyzing the results of each reuse cycle, observed that it has been achieved 100 % degradation in every case, indicating that the nanostructures remain effective without significant loss of performance. Furthermore, in terms of degradation kinetics, the coefficient obtained is $k = 0.1301\ h^{-1}$, $k = 0.2287\ h^{-1}$ and $k = 0.1792\ h^{-1}$ for each respective cycle.

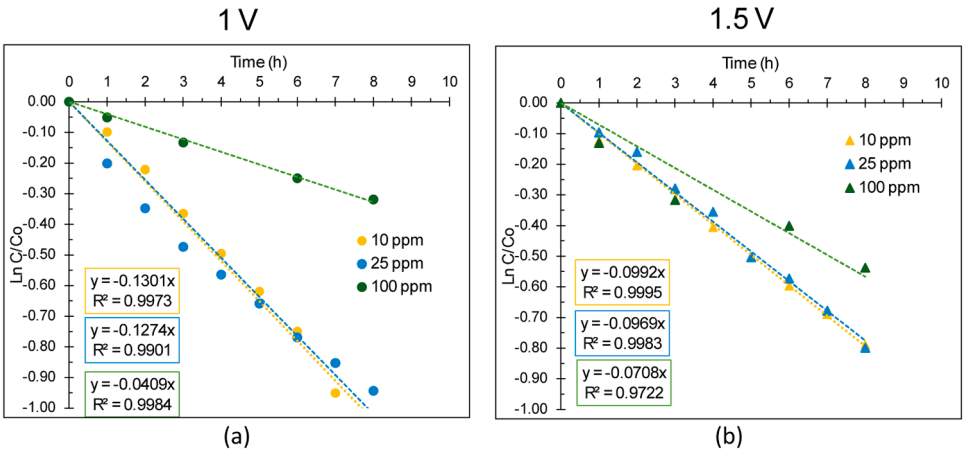

Fig. 7. DEP photoelectrocatalyc degradation kinetics varying the initial concentration of DEP (10 ppm, 25 ppm and 100 ppm) (a) at 1 V and (b) at 1.5 V.

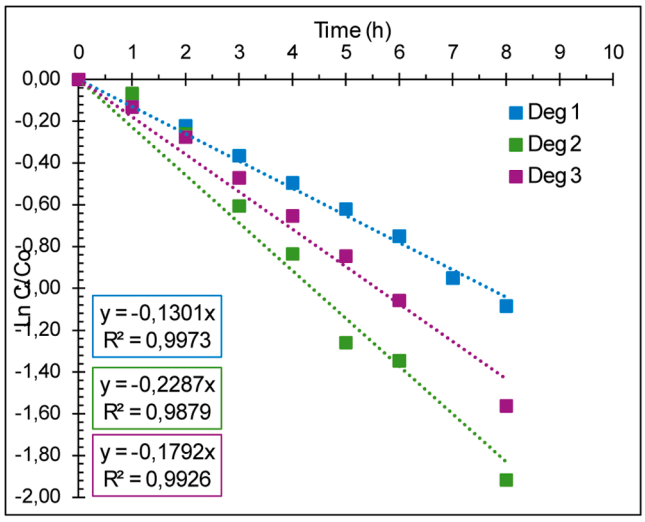

Fig. 8. DEP photoelectrocatalyc degradation kinetics re-using the WO3 nanostructures three times applying 1 V during the degradation and using 10 ppm as initial concentration of DEP.

To contextualize the number of reuse cycles, it is worth noting that many studies on metal oxide-based photocatalysts report 3 to 5 cycles as standard. For example, TiO_2 films [39], K_2O/SiO_2 [40], and WO_3/SiO_2 monoliths [41] have shown stable performance within this range. Our choice of three cycles is thus consistent with common practice and sufficient to demonstrate the material's good initial reusability. Additionally, a 1-hour continuous operation test (Figure S1, Supporting Information) further confirms the stability of the WO_3 nanostructures under extended photoelectrocatalytic conditions.

Overall, these findings suggest that WO_3 nanostructures are both stable and reusable over multiple cycles, maintaining high degradation efficiency with minimal impact on the rate constant. This reusability makes WO_3 a viable candidate for sustainable pollutant degradation applications.

3.4. Degradation intermediates of diethyl phthalate (DEP)

Apart from assessing the degradation efficiency and kinetics for the degradation of DEP, thanks to the UHPLCS-MS/MS intermediate compounds formed during its degradation could be identified. These compounds were identified based on the mass spectra obtained from the Base Peak Chromatogram (BPC) of the degradation process (Figure S5) and bibliographic references [38,42–44]. Figure S5 shows the BPC of the samples taken during the 24 h degradation. The peak corresponding to DEP is observed (tr = 12.4 min) and different peaks that are associated to degradation intermediates of DEP. Table 2 shows the intermediate compound identified and its characteristics and Fig. 9 shows the exact ion chromatogram (EIC) of the different intermediates of degradation found.

Using the EIC data, the concentration trends of each identified intermediate compound were plotted over the DEP degradation process (Figure S6). It was observed that only Intermediate 1 disappears after 5 h of testing. In contrast, the other intermediates could be considered as final degradation products since they remain in the sample after 24 h of degradation. More specifically, Intermediates 2, 3, 5, 7, 8, and 9 display a decreasing trend, suggesting that they would eventually disappear if the photoelectrochemical degradation process were prolonged. However, Intermediates 4, 6, and 10 exhibit either a stable or increasing trend in the 24-hour sample, suggesting that they could be considered as final degradation products. After conducting this study, a degradation pathway for DEP was proposed, as shown in Fig. 10.

The DEP degradation pathway involves hydroxylation, structural rearrangement of the aromatic ring, and oxidation of specific compounds, ultimately leading to the formation of smaller compounds. The degradation pathway is described in detail below. DEP initially undergoes hydroxylation through the addition of a hydroxyl group to the phthalate ring, forming Intermediate 1. Next, Intermediate 1 undergoes a second hydroxylation, resulting in Intermediate 2, where an additional hydroxyl group is added to the ring. Intermediate 2 then undergoes a final hydroxylation, producing Intermediate 3 with a third hydroxyl group in the structure.

Table 2
Intermediate compounds identified in the photoelectrochemical degradation of DEP.

Component identifier	Component	Molecular formular	Retention time (min)	*m/z* value
1	diethyl 4-hydroxyphthalate	$C_{12}H_{14}O_5$	11	239,0965
2	diethyl 4,5-dihydroxyphthalate	$C_{12}H_{14}O_6$	16,8	255,1350
3	diethyl 3,4,5-trihydroxyisobutylate	$C_{12}H_{14}O_7$	19	272,2580
4	5-Hydroxyisobenzofuran-1,3-dione	$C_8H_4O_4$	27,5	163,9686
5	5,6-dihydroxyisobenzofuran-1,3-dione	$C_8H_4O_5$	28	181,0613
6	3,4-dihydroxybenzo[c] oxepin-1,5-dione	$C_{10}H_8O_3$	12,4	177,0546
7	7-oxabicyclo[4,2,0]octa-1,3,5-trien-8-one	$C_7H_4O_2$	12,5	120,9708
8	3,4,5,6-tetrahydrobenzo	$C_{12}H_{12}O_4$	24,1	221,1386
9	Benzoic acid	$C_7H_6O_2$	27,4	122,9420
10	Succinic acid	$C_4H_6O_4$	1	118,0862

Following the initial hydroxylation (Intermediate 1), the alkyl groups are cleaved, and the atoms rearrange to form a new cyclic structure consisting of a benzofuran ring (Intermediate 4). Intermediate 5 is produced through further hydroxylation of Intermediate 4. Subsequently, Intermediate 6 forms from Intermediate 5 through an intramolecular cyclization, creating a new ring and resulting in an oxepinone-dione system. This process may involve the elimination of a hydroxyl group and the formation of a new carbon-carbon bond to stabilize the oxepinone structure. The degradation process of DEP continues through cyclization and formation of oxygenated compounds. Intermediate 7 may arise from ring contraction of Intermediate 6, as Intermediate 6 is relatively unstable.

Intermediate 8 retains the original structure, suggesting it could be formed directly from DEP or from the hydroxylated compounds (Intermediates 1, 2, and 3). The formation of Intermediate 8 involves the loss of hydroxyl groups in Intermediates 1, 2, and 3, and closure of the ring through the binding of alkyl chains.

Finally, as the degradation advances, intermediate products fragment into smaller carboxylic acids and simpler molecules, such as Intermediate 9 and Intermediate 10.

4. Conclusions

This work supports defect engineering as a viable approach to improve the efficiency of WO_3 nanostructures for environmental applications, such as wastewater treatment. Scaling of the WO_3 nanostructure from 0.5 cm^2 to 15 cm^2 has been successful, maintaining and even improving the DEP degradation efficiency. The introduction of defects by controlled reduction for 5 min has proven to be an effective method to optimize the photoelectrocatalytic activity, allowing the material to scale up without loss of performance. This is a significant advance for large-scale environmental applications, as it confirms the feasibility of amorphous WO_3 nanostructures for organic pollutant treatment processes on larger surfaces.

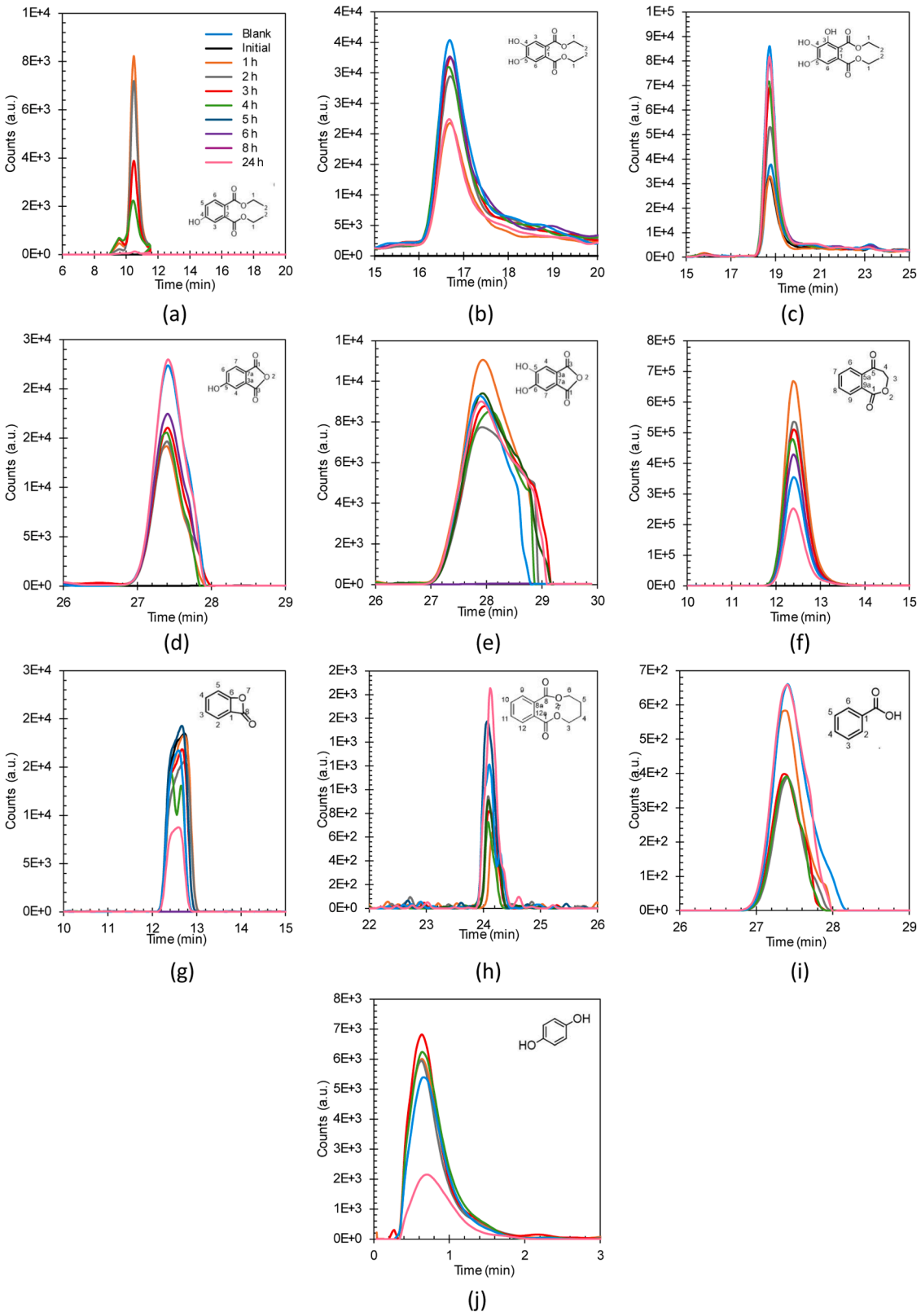

Fig. 9. Identified intermediates EIC for the degradation of DEP. (a) Intermediate 1 ($m/z = 239{,}0965$) (b) Intermediate 2 ($m/z = 255{,}1350$) (c) Intermediate 3 ($m/z = 272{,}2580$) (d) Intermediate 4 ($m/z = 163{,}9686$) (e) Intermediate 5 ($m/z = 181{,}0613$) (f) Intermediate 6 ($m/z = 177{,}0546$) (g) Intermediate 7 ($m/z = 120{,}9708$) (h) Intermediate 8 ($m/z = 221{,}1386$) (i) Intermediate 9 ($m/z = 112{,}9420$) y (j) Intermediate 10 ($m/z = 118{,}0862$).

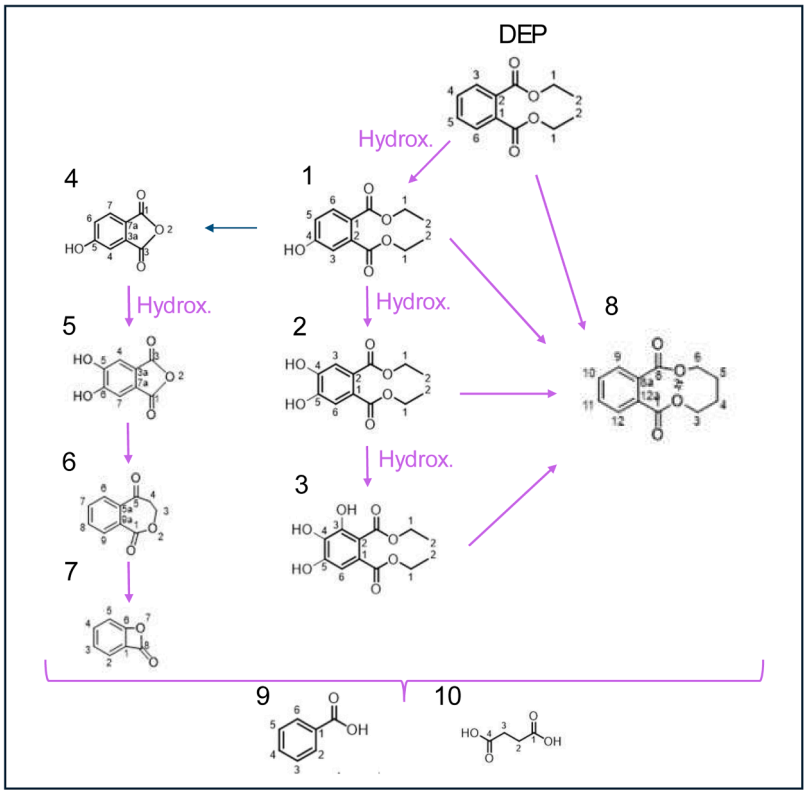

Fig. 10. DEP degradation pathway.

The photoelectrochemical degradation conditions were optimized at 1 V and an initial contaminant concentration of 10 ppm (DEP), resulting in a degradation constant (k) of 0.1301 h^{-1}. Additionally, the reusability tests confirmed the high stability of the nanostructures achieving 100 % degradation across three cycles with only minor variations in kinetic constants (k = 0.1301 h^{-1}, 0.2287 h^{-1}, and 0.1792 h^{-1}), reinforcing the suitability of WO_3 nanostructures for sustainable, long-term pollutant degradation. Compared to conventional photocatalysis or electrocatalysis using WO_3, the photoelectrocatalytic system offers enhanced charge separation, improved radical generation, and better degradation kinetics under moderate conditions. These features make PEC a more efficient and scalable approach for pollutant removal using WO_3-based materials.

Additionally, UHPLC-MS analysis identified 10 intermediate compounds formed during the DEP degradation process. The proposed degradation pathway involves hydroxylation, structural rearrangement of the aromatic ring, and oxidation of specific compounds, leading to the formation of smaller degradation products. The findings offer valuable insights into the degradation mechanism of DEP and highlight the potential of WO_3 nanostructures for efficient and sustainable water treatment.

Future work will focus on applying this system to real wastewater matrices and on post-treatment characterization of the nanostructures to evaluate structural changes during degradation.

CRediT authorship contribution statement

M. Cifre-Herrando: Writing – original draft, Visualization, Software, Resources, Methodology, Investigation, Formal analysis, Data curation, Conceptualization. **G. Roselló-Márquez:** Writing – review & editing, Validation, Supervision. **J. García-Antón:** Writing – review & editing, Validation, Investigation, Funding acquisition. **L. Mais:** Writing – review & editing, Validation, Investigation, Supervision. **M. Mascia:** Writing – review & editing, Validation, Investigation, Supervision.

Declaration of competing interest

The authors declare that they have no known competing financial interests or personal relationships that could have appeared to influence the work reported in this paper.

Acknowledgments

The authors wish to thank the economic support granted by AEI (PID2019–105844RB-I00/AEI/10.13039/501100011033). M. Cifre-Herrando acknowledges the Ministerio de Universidades for the predoctoral grant (FPU19/02466). G. Roselló-Márquez is also grateful to UPV for the post-doctoral grant (PAID-10–21) and the grant to support postdoctoral research at UPV (PAID-PD-22). Additionally, funding from the Spanish Research Network E3TECH-PLUS (RED2022–134552-T, MICINN/AEI) is acknowledged.

Supplementary materials

Supplementary material associated with this article can be found, in the online version, at doi:10.1016/j.electacta.2025.146706.

References

[1] H. Zúñiga-Benítez, A. Muñoz-Calderón, G.A. Peñuela, Removal of a mix of benzophenones and parabens using solar photo-fenton and a cylinder parabolic collector in aqueous solutions, J. Environ. Chem. Eng. 6 (2018) 7347–7357, https://doi.org/10.1016/J.JECE.2018.08.039.

[2] G. Liu, W. Cai, H. Liu, H. Jiang, Y. Bi, H. Wang, The association of bisphenol A and phthalates with risk of breast cancer: a meta-analysis, Int. J. Environ. Res. Public Health 18 (2021) 2375, https://doi.org/10.3390/ijerph18052375.

[3] S. Siddique, C. Kubwabo, S.A. Harris, A review of the role of emerging environmental contaminants in the development of breast cancer in women, Emerg. Contam. 2 (2016) 204–219, https://doi.org/10.1016/j.emcon.2016.12.003.

[4] F.-P. Chen, M.-H. Chien, Lower concentrations of phthalates induce proliferation in human breast cancer cells, Climacteric. 17 (2014) 377–384, https://doi.org/10.3109/13697137.2013.865720.

[5] P. Agilandeswari, S. Venkateshbabu, N. Rajamohan, G. Sarojini, M. Rajasimman, Synthesis and functional mechanism evaluation of novel polymer-graphene oxide-biochar nanocomposite for efficient removal of diethyl phthalate, Environ. Res. 263 (2024), https://doi.org/10.1016/j.envres.2024.120032.
[6] Z. Chai, X. Bi, H. Jia, Use of typical wastes as biochars in removing diethyl phthalate (Det) from water, Processes 10 (2022), https://doi.org/10.3390/pr10071369.
[7] M. Carolina de Almeida, M.R. Machado, G.G. Costa, G.A.R. de Oliveira, H.F. Nunes, D.F. Maciel Costa Veloso, T.A. Ishizawa, J. Pereira, T. Ferreira de Oliveira, Influence of different concentrations of plasticizer diethyl phthalate (DEP) on toxicity of Lactuca sativa seeds, Artemia salina and Zebrafish, Heliyon. (2023), https://doi.org/10.1016/j.heliyon.2023.e18855, 9.
[8] S. Zhang, J. Wei, N. Wu, A.A. Allam, J.S. Ajarem, S. Maodaa, Z. Huo, F. Zhu, R. Qu, Assessment of the UV/DCCNa and UV/NaClO oxidation process for the removal of diethyl phthalate (DEP) in the aqueous system, Environ. Pollut. 341 (2024), https://doi.org/10.1016/j.envpol.2023.122915.
[9] M. Shi, X. Wang, M. Shao, L. Lu, H. Ullah, H. Zheng, F. Li, Resource utilization of typical biomass wastes as biochars in removing plasticizer diethyl phthalate from water: characterization and adsorption mechanisms, Front. Environ. Sci. Eng. 17 (2023), https://doi.org/10.1007/s11783-023-1605-4.
[10] European Chemicals Agency, Endocrine disruptor assessment List, (2023). https://echa.europa.eu/es/ed-assessment (accessed May 7, 2024).
[11] A. Giwa, A. Yusuf, H.A. Balogun, N.S. Sambudi, M.R. Bilad, I. Adeyemi, S. Chakraborty, S. Curcio, Recent advances in advanced oxidation processes for removal of contaminants from water: a comprehensive review, Process Saf. Environ. Prot. 146 (2021) 220–256, https://doi.org/10.1016/j.psep.2020.08.015.
[12] S. Garcia-Segura, E. Brillas, Applied photoelectrocatalysis on the degradation of organic pollutants in wastewaters, J. Photochem. Photobiol. C: Photochem. Rev. 31 (2017) 1–35, https://doi.org/10.1016/j.jphotochemrev.2017.01.005.
[13] R. Wang, X. Ma, T. Liu, Y. Li, L. Song, S.C. Tjong, L. Cao, W. Wang, Q. Yu, Z. Wang, Degradation aspects of endocrine disrupting chemicals: a review on photocatalytic processes and photocatalysts, Appl. Catal. Gen. 597 (2020), https://doi.org/10.1016/j.apcata.2020.117547.
[14] Y. Liu, Y. Li, W. Li, S. Han, C. Liu, Photoelectrochemical properties and photocatalytic activity of nitrogen-doped nanoporous WO 3 photoelectrodes under visible light, Appl. Surf. Sci. 258 (2012) 5038–5045, https://doi.org/10.1016/j.apsusc.2012.01.080.
[15] A. Tolosana-Moranchel, S. McMichael, J.W.J. Hamilton, J.A. Byrne, P. Fernández-Ibañez, Electrochemically assisted photocatalytic degradation of contaminants of emerging concern in simulated wastewater using WO3 – Elucidation of mechanisms, Chem. Eng. J. 458 (2023), https://doi.org/10.1016/j.cej.2023.141442.
[16] G. Roselló-Márquez, R.M. Fernández-Domene, R. Sánchez-Tovar, J. García-Antón, Photoelectrocatalyzed degradation of organophosphorus pesticide fenamiphos using WO3 nanorods as photoanode, Chemosphere 246 (2020), https://doi.org/10.1016/j.chemosphere.2019.125677.
[17] M. Cifre-Herrando, G. Roselló-Márquez, D.M. García-García, J. García-Antón, Degradation of Methylparaben using optimal WO3 nanostructures: influence of the annealing conditions and complexing agent, Nanomaterials 12 (2022), https://doi.org/10.3390/nano12234286.
[18] M. Cifre-Herrando, G. Roselló-Márquez, J. García-Antón, Is photoelectrocatalysis an efficient process to degrade endocrine disruptors chemicals? Environ. Toxicol. Pharmacol. 107 (2024) https://doi.org/10.1016/j.etap.2024.104420.
[19] G. Rosello-Marquez, R.M. Fernandez-Domene, R. Sanchez-Tovar, M. Cifre-Herrando, J. Garcia-Anton, Degradation of Diazinon based on photoelectrocatalytic technique using enhanced WO3nanostructures: mechanism and pathway, J. Environ. Chem. Eng. 9 (2021), https://doi.org/10.1016/j.jece.2021.105371.
[20] P. Mahbub, M. Duke, Scalability of advanced oxidation processes (AOPs) in industrial applications: a review, J. Environ. Manage. 345 (2023), https://doi.org/10.1016/j.jenvman.2023.118861.
[21] V.H.V. Quy, I.R. Jo, S.H. Kang, K.S. Ahn, Amorphous-crystalline dual phase WO3 synthesized by pulsed-voltage electrodeposition and its application to electrochromic devices, J. Ind. Eng. Chem. 94 (2021) 264–271, https://doi.org/10.1016/j.jiec.2020.10.047.
[22] Y. Zhang, X. Liang, T. Jiang, H. Liu, Y. Fu, D. Zhang, Z. Geng, Amorphous/crystalline WO3 dual phase laminated films: fabrication, characterization and evaluation of their electrochromic performance for smart window applications, Sol. Energy Mater. Sol. Cells 244 (2022), https://doi.org/10.1016/j.solmat.2022.111820.
[23] Y. Shi, M. Sun, Y. Zhang, J. Cui, Y. Wang, X. Shu, Y. Qin, H.H. Tan, J. Liu, Y. Wu, Structure modulated amorphous/crystalline WO3 nanoporous arrays with superior electrochromic energy storage performance, Sol. Energy Mater. Sol. Cells 212 (2020), https://doi.org/10.1016/j.solmat.2020.110579.
[24] Y. Li, M. Je, J. Kim, C. Xia, S.H. Roh, W. So, H. Lee, D.H. Kim, S.M. Cho, J.W. Bae, H. Choi, J.K. Kim, Rational nanopositioning of homogeneous amorphous phase on crystalline tungsten oxide for boosting solar water oxidation, Chem. Eng. J. 438 (2022), https://doi.org/10.1016/j.cej.2022.135532.
[25] S. Anantharaj, S. Noda, Amorphous catalysts and electrochemical water splitting: an untold story of harmony, Small. 16 (2020), https://doi.org/10.1002/smll.201905779.
[26] M. Szkoda, Z. Zarach, K. Trzciński, A.P. Nowak, An aqueous exfoliation of wo3 as a route for counterions fabrication—Improved photocatalyticand capacitive properties of polyaniline/wo3 composite, Mater. (Basel) 13 (2020) 1–16, https://doi.org/10.3390/ma13245781.
[27] W. Cai, R. Chen, H. Yang, H.B. Tao, H.Y. Wang, J. Gao, W. Liu, S. Liu, S.F. Hung, B. Liu, Amorphous versus crystalline in water oxidation catalysis: a case study of NiFe alloy, Nano Lett. 20 (2020) 4278–4285, https://doi.org/10.1021/acs.nanolett.0c00840.
[28] S. Lv, J. Wang, The technical support of nanoart: anodization process, Anti-Corros. Methods Mater. 66 (2019) 242–250, https://doi.org/10.1108/ACMM-08-2017-1826.
[29] Erik. Lassner, W.-Dieter. Schubert, Tungsten : Properties, Chemistry, Technology of the Element, Alloys, and Chemical Compounds, Kluwer Academic/Plenum Publishers, 1999.
[30] Y. Zhao, S. Balasubramanyam, R. Sinha, R. Lavrijsen, M.A. Verheijen, A.A. Bol, A. Bieberle-Hütter, Physical and chemical defects in WO3 thin films and their impact on photoelectrochemical water splitting, ACS. Appl. Energy Mater. 1 (2018) 5887–5895, https://doi.org/10.1021/acsaem.8b00849.
[31] S.B. Upadhyay, R.K. Mishra, P.P. Sahay, Enhanced acetone response in co-precipitated WO3 nanostructures upon indium doping, Sens. Actuators. B Chem. 209 (2015) 368–376.
[32] R.H. Acuña, J.L. Romero, E.M.R. Muñoz, E.R. Francis, B.C. Cedeño, F.P. Delgado, Síntesis Hidrotérmica de Nanoestructuras de Óxido de Tungsteno (WO3) Monoclínico, in: Proceedings of the Memorias Del XXXIV Encuentro Nacional y III Congreso Internacional de La AMIDIQ, Mazatlán, México, 2013, pp. 7–10.
[33] A. Chakib, K. Mohamed, A. Elaziouti, W. Touati, I. Kaddi Allah, A. Benhamed, A. Bekka, Solvothermal synthesis and characterization of monoclinic WO 3 nanoplatelets. Investigation of their photocatalytic performance, (2022). https://doi.org/10.21203/rs.3.rs-1886856/v1.
[34] Y. Cui, F. Liang, C. Ji, S. Xu, H. Wang, Z. Lin, J. Liu, Discoloration effect and one-step synthesis of hydrogen tungsten and molybdenum bronze (H x MO 3) using liquid metal at room temperature, ACS. Omega 4 (2019) 7428–7435, https://doi.org/10.1021/acsomega.9b00840.
[35] L. Jin, Q. Zhang, R.J. Cava, The hydrogen-containing bronzes H0.23WO3 and H0.10ReO3 synthesized via a polymer route, J. Solid. State Chem. 297 (2021), https://doi.org/10.1016/j.jssc.2021.122059.
[36] A.M. Polcaro, A. Vacca, M. Mascia, S. Palmas, R. Pompei, S. Laconi, Characterization of a stirred tank electrochemical cell for water disinfection processes, Electrochim. Acta 52 (2007) 2595–2602, https://doi.org/10.1016/j.electacta.2006.09.015.
[37] L. Mais, M. Mascia, S. Palmas, A. Vacca, Photoelectrochemical oxidation of phenol with nanostructured TiO2-PANI electrodes under solar light irradiation, Sep. Purif. Technol. 208 (2019) 153–159, https://doi.org/10.1016/j.seppur.2018.03.074.
[38] T.K. Lau, W. Chu, N. Graham, The degradation of endocrine disruptor di-n-butyl phthalate by UV irradiation: a photolysis and product study, Chemosphere 60 (2005) 1045–1053, https://doi.org/10.1016/j.chemosphere.2005.01.022.
[39] B. Barrocas, O.C. Monteiro, M.E.M. Jorge, S. Sério, Photocatalytic activity and reusability study of nanocrystalline TiO 2 films prepared by sputtering technique, Appl. Surf. Sci. 264 (2013) 111–116, https://doi.org/10.1016/j.apsusc.2012.09.136.
[40] R.S.R.M. Hafriz, I. Nor Shafizah, N.A. Arifin, A.H. Maisarah, A. Salmiaton, A. H. Shamsuddin, Comparative, reusability and regeneration study of potassium oxide-based catalyst in deoxygenation reaction of WCO, Energy Convers. Manag.: X 13 (2022), https://doi.org/10.1016/j.ecmx.2021.100173.
[41] S. Sharma, S. Basu, Highly reusable visible light active hierarchical porous WO3/SiO2 monolith in centimeter length scale for enhanced photocatalytic degradation of toxic pollutants, Sep. Purif. Technol. 231 (2020), https://doi.org/10.1016/j.seppur.2019.115916.
[42] B. Xu, N.Y. Gao, X.F. Sun, S.J. Xia, M. Rui, M.O. Simonnot, C. Causserand, J. F. Zhao, Photochemical degradation of diethyl phthalate with UV/H2O2, J. Hazard. Mater. 139 (2007) 132–139, https://doi.org/10.1016/j.jhazmat.2006.06.026.
[43] L. Mansouri, C. Tizaoui, S.U. Geissen, L. Bousselmi, A comparative study on ozone, hydrogen peroxide and UV based advanced oxidation processes for efficient removal of diethyl phthalate in water, J. Hazard. Mater. 363 (2019) 401–411, https://doi.org/10.1016/j.jhazmat.2018.10.003.
[44] M. Muneer, J. Theurich, D. Bahnemann, Titanium dioxide mediated photocatalytic degradation of 1,2-diethyl phthalate, 2001.